CHEMISTRY OF MATERIALS

pubs.acs.org/cm

Article

Stabilizing Effects of Phosphorus-Doped Silicon Nanoparticle Anodes in Lithium-Ion Batteries

Isabelle P. Gordon, Wei Xu, Sophia Randak, T. Richard Jow, and Nicholas P. Stadie*

Cite This: *Chem. Mater.* 2023, 35, 549−557

Read Online

ACCESS | Metrics & More | Article Recommendations | Supporting Information

ABSTRACT: Phosphorus-doped silicon has been reported to exhibit improved cycling stability and/or higher capacity retention than pure silicon as the anode in lithium-ion batteries. However, crystallite size and particle morphology are difficult to decouple from compositional tuning during chemical modification. In this work, we explore direct solid-state routes to phosphorus doping of silicon powders relevant to electrochemical applications. A wide range of compositions are assessed, from 0.05 to 3.0 at % P, as well as a wide range of silicon starting materials of varying crystallinity, particle size, and particle morphology. Successful incorporation of phosphorus into the silicon lattice is best confirmed by X-ray diffraction; the Si(111) reflection shifts to higher angles as consistent with the known lattice contraction of 0.002 Å per 1 at % phosphorus. The addition of phosphorus to Si nanoparticles (100−500 nm) in the high doping regime causes grain coarsening and catalyzes an increase in crystallinity. On the other hand, dilute doping of phosphorus can be carried out without great alteration of the nanoparticulate morphology. The opposite effect occurs for very large microparticles (>10 μm), whereby the doping is concomitant with a disruption of the crystal lattice and reduction of the crystallite size. These effects are borne out in both the electrochemical stability over long-term cycling in a lithium-ion half-cell as well as in the thermal stability under high-temperature decomposition. By comparison across a wide range of pure and P-doped materials of varying particle and crystallite sizes, the independent effects of doping and structure on thermal and electrochemical stability are able to be decoupled herein. A stabilizing effect is most significant when phosphorus doping is dilute and heterogeneous (surface-enriched) within the silicon nanoparticles.

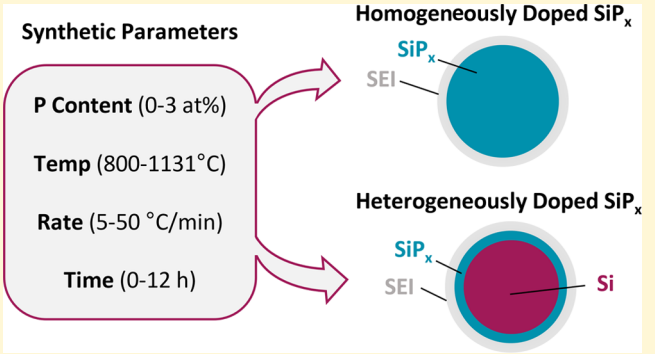

1. INTRODUCTION

Silicon is a promising next-generation anode material for lithium-ion batteries (LIBs) owing to its high theoretical capacity (3579 mAh g^{-1} for lithiation to $Li_{15}Si_4$) and high abundance in Earth's crust; however, many challenges remain in realizing its widespread use in commercial batteries mainly related to its large volume expansion (>300%) upon lithiation, causing subsequent pulverization of the electrode, loss of electrical contact, and solid-electrolyte interphase (SEI) instability.[1] Strategies such as nanosizing[2−4] or employing unique morphologies (e.g., Si needles[5,6]) as well as embedding the Si phase within a buffering matrix (e.g., Si−C composites)[7,8] have been explored as ways to mitigate troublesome volume expansion/contraction during cycling. Nevertheless, in all cases, the reactivity of pure silicon with carbonate-based electrolytes commonly employed in LIBs remains an important safety issue, potentially leading to catastrophic thermal runaway.[9−11] Extensive efforts have also been made to tailor the electrolyte for increased stability during cycling,[12−14] especially by the use of solid-state electrolytes.[15] An alternative strategy is to passivate the silicon electrode interface using artificial SEI or by chemical doping of silicon itself. Numerous chemical dopants have been proposed in the latter strategy, including p-block elements such as boron,[16−18] nitrogen,[19] phosphorus,[8,20−24] and sulfur,[25] and metals such as Mg, Al, Ca, and Zn.[26,27] Nevertheless, it generally remains unclear whether elemental substitution is the primary cause of any resulting electrochemical or thermal stabilization effects.

The elements with the highest equilibrium solubility in silicon are arsenic (up to ∼3.6 at %), phosphorus (up to ∼3.0 at %), and boron (up to ∼1.2 at %).[28] Phosphorus and boron are well-known dopants of silicon in the semiconductor industry owing to their electron-donating and electron-withdrawing (n- and p-type doping) characters, respectively, and both significantly increase their electrical conductivity.[29,30] Arsenic is not a likely candidate for technological applications; hence, to achieve the widest range of substitutional doping

Received: September 29, 2022
Revised: December 20, 2022
Published: January 3, 2023

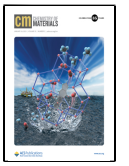

possible, phosphorus is the most suitable candidate for determining the role of substitutional doping on the materials and electrochemical properties of silicon. Past investigations of phosphorus-doped silicon electrodes have focused on doping as-deposited films[20] or by facile but imprecise ball-milling techniques.[8,31] In many cases, composite structures combined with heteroatom doping have been combined to combat the above issues associated with silicon during electrochemical cycling.[8,22,23] For example, ball-milling of phosphorus-doped silicon and graphite resulting in a composite material with low charge-transfer resistance and long cyclability and stability was explored.[8] Similarly, ball-milling of silicon, black phosphorus, and MWCNTs shows high reversible capacity (>2000 mAh g^{-1}) and reduced volume expansion during cycling.[31] Such synergistic effects mask the effects due exclusively to chemical doping.

The investigations described herein aim to shed light on whether substitutional chemical doping, using phosphorus as the dopant, can be used to tailor the electrochemical and thermal properties of silicon nanoparticles (NPs) toward their application as a LIB anode material in the presence of a standard carbonate-based liquid electrolyte. Electrode fabrication via casting of aqueous slurries in air using standard methods was chosen as the method of interest for highest relevance to existing LIB manufacturing procedures; a top-down approach to phosphorus doping of the NPs prior to electrode fabrication was used. In this way, the resulting changes in silicon composition, structure, and morphology could be systematically controlled for by investigation of a wide range of materials prepared under different dissolution conditions. The results of this analysis give rise to basic guiding principles as to the use of phosphorus as a substitutional dopant in silicon electrodes, providing a foundation for further optimization of electrochemical cells and further exploration of suitable dopants.

2. EXPERIMENTAL METHODS

2.1. Preparation of Solid Solutions (SiP_x). The solid precursors, silicon powder and stabilized red phosphorus powder (8.07270, Sigma-Aldrich), were mixed together by a mortar and pestle under Ar atmosphere inside a glovebox (<0.5 ppm H_2O/O_2). Three silicon powders were explored in this work as the silicon precursor: 100 nm Si NPs (98%, 633097, lot# MKCM0616, Sigma-Aldrich), 500 nm Si NPs (99.995%, US5011, U.S. Research Nanomaterials Inc.), and 44 μm Si microparticles (MPs, 99%, 215619, lot# MKCK6629, Sigma-Aldrich). Multiple dilutions were performed at no higher than 10:1 in any given step to ensure homogeneity of mixing; mixing was performed for 5 min per step. The powder mixture was then transferred into a custom-made quartz ampule (0.8 cm inner diameter, 20 cm length), and a Swagelok ultra-torr adaptor was placed over the opening. The ampule was flame sealed at the preformed neck under rough vacuum. The ampule was then placed on an elevated rack at the center of a chamber furnace (CWF12/13, Carbolite-Gero) and heated to a final hold temperature via a PID controller (Eurotherm 3216) for a specified hold time via a specified ramp rate. Temperature set point (800 or 1131 °C, L or H, respectively), hold time (0, 1, 6, 12 h), and ramp rate (5, 10, 20, 30, 50 °C min^{-1}) were varied accordingly. Finally, the samples were cooled by natural convection to below 100 °C and then opened using a diamond-bladed rotary saw under air. The so-obtained materials were analyzed or further used as collected (without washing). They are referred to herein by their nominal concentration (e.g., 0.1 at % SiP_x = 0.1P), temperature set point (e.g., 1131 °C = H), hold time (e.g., 1 h = 1h), and ramp rate (e.g., 10 °C min^{-1} = 10R), as shown in Table S1.

2.2. Materials Characterization. Powder X-ray diffraction (XRD) measurements were performed using a Bruker D8 Advance diffractometer with Cu $K\alpha_{1,2}$ radiation (λ = 1.54 Å) in Bragg–Brentano geometry. Samples were prepared by physically mixing with a corundum (Al_2O_3) internal standard and mounted on an oriented silicon crystal (low background) holder. Raman spectroscopy was performed using an HR Evolution spectrometer (Horiba Scientific Ltd.) equipped with a confocal microscope using a 532 nm (2.33 eV) frequency-doubled Nd:YAG laser with an incident power of 45 mW. Two types of Raman measurements, referred to as "surface" and "bulk," were collected by adjusting the focal point to ±10 μm from the plane of focus with maximum intensity. Scanning electron microscopy (SEM) was performed using a Zeiss Supra 55VP microscope, operated at 1 kV. Samples were prepared for SEM by spreading a small quantity of powder onto a conductive carbon tape. Electrical conductivity was measured under compression within a custom guard electrode setup using a Keithley 2450 sourcemeter as described elsewhere.[32]

2.3. Electrode Materials. The following materials were used in the preparation of electrochemical cells: lithium hexafluorophosphate ($LiPF_6$, battery grade, Gotion Inc.), ethylene carbonate (EC, battery grade, Gotion Inc.), dimethyl carbonate (DMC, battery grade, Gotion Inc.), fluoroethylene carbonate (FEC, battery grade, Gotion Inc.), lithium metal (chips, 99.9%, MTI Corp.), glass microfiber disks (0.67 × 257 mm^2, GF/D grade, catalogue number 1823-257, Whatman), carbon black (Super P, Timcal Ltd.), carboxymethyl cellulose (CMC, batch #0011912, MTI), and copper foil (thickness 9 μm, MTI Corp.).

2.4. Electrode Fabrication. Slurries were prepared by mixing SiP_x active material (80 wt %), conductive additive (Super P, 10 wt %), and binder (CMC, 10 wt %) in deionized water using an automatic mixer (Thinky AR-100). The slurry was cast onto a Cu foil using a doctor blade and then subjected to a three-stage drying protocol: under air at room temperature for 8 h, under air at 80 °C for a further 8 h, and then lastly under rough vacuum (Welch Chemstar Dry 2071B) at 100 °C for a further 10 h. Electrodes were punched into disks with a diameter of 10 mm, and then stored under argon in a glovebox (<0.1 ppm H_2O/O_2) until further use. Homogeneous loadings of 0.75–1.00 mg cm^{-2} were achieved across all electrodes reported herein.

2.5. Electrochemical Cell Fabrication. Half-cells were assembled under argon atmosphere in a glovebox (<0.1 ppm H_2O/O_2) in coin-cell format (316 stainless steel, size 2032, Xiamen AOT Electronics Technology Co.). An above-described SiP_x electrode served as the working electrode, a glass microfiber disk as the separator (16 mm diameter), and a Li chip as the counter electrode; the cell was flooded with 125 μL of 1.0 M $LiPF_6$ in EC/DMC (1:1 by weight) with 2 wt % FEC as the electrolyte and then closed.

2.6. Electrochemical Measurements. Galvanostatic charge/discharge cycling was performed in a temperature-controlled incubator (KB 53, Binder GmbH) at 25.0 °C using a battery cycler (CT30001A, Landt Instruments). Charge and discharge were performed using a constant current (CC) protocol at 1 A g^{-1} within the voltage range of 0.05–1.5 V vs Li^+/Li.

3. RESULTS

3.1. Homogeneous SiP_x Solid Solutions. Homogeneously doped solid solutions of phosphorus in silicon (SiP_x between 0.05 and 3.0 at % P) were first prepared via solid-state chemical reaction between large silicon NPs (of nominal size of 500 nm) and red phosphorus in a closed ampule under vacuum. The hold temperature of dissolution (1131 °C) was initially held constant between all samples and chosen based on the eutectic temperature between the Si solid solution and binary SiP, the equilibrium point of maximum solubility in Si.[33] A ramp rate of 5 °C min^{-1} and a hold time of 1 h were found to be sufficient (the latter originally estimated based on diffusion rates[34,35] of P in Si). Upon opening the ampule in air, no further reaction of the product occurred, indicating that the

https://doi.org/10.1021/acs.chemmater.2c02983
Chem. Mater. 2023, 35, 549–557

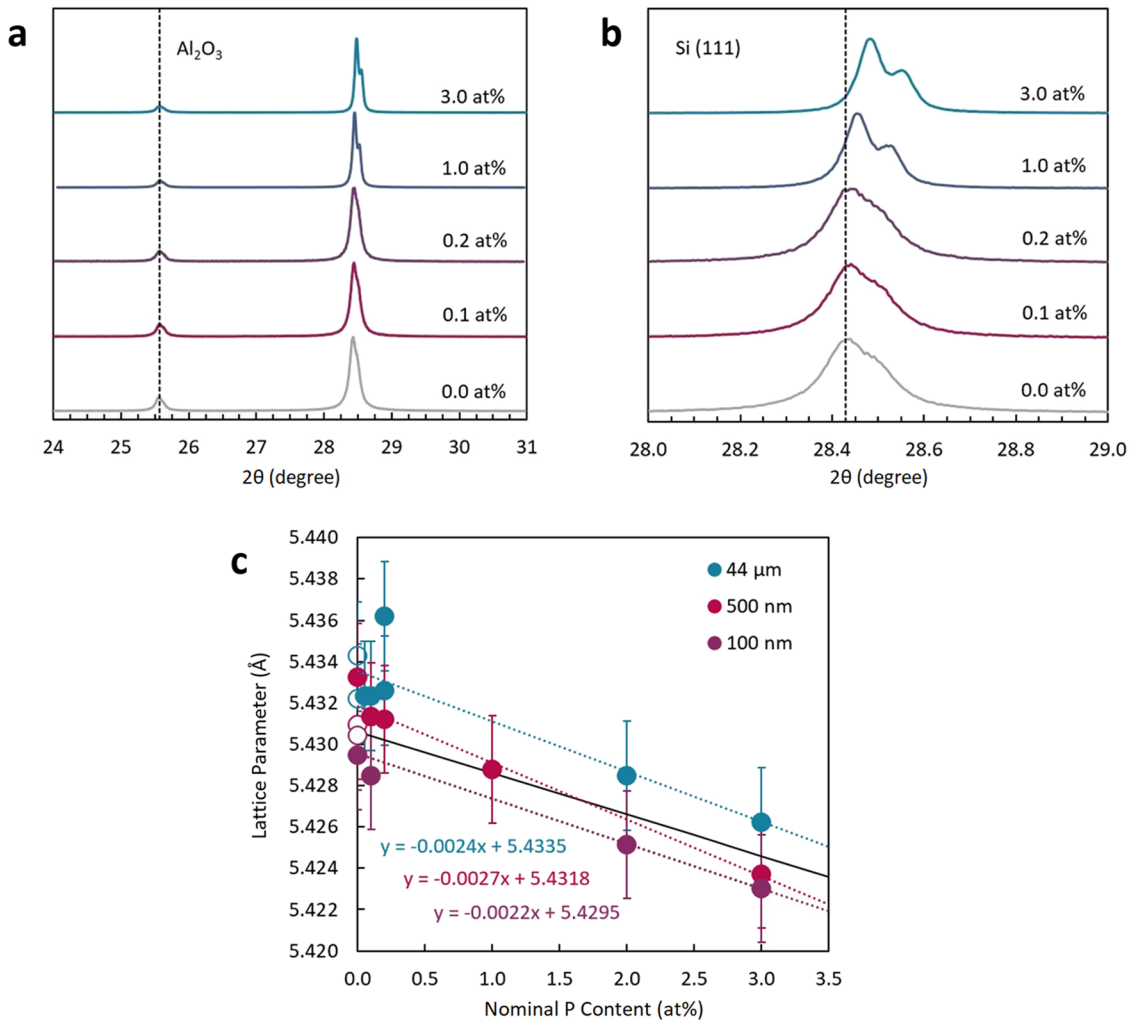

Figure 1. (a) XRD patterns of SiP_x (from 500 nm Si NP precursor) with nominal P content between 0.1 and 3.0 at % physically mixed with an internal corundum standard. (b) Details of the Si(111) XRD peak. (c) Lattice parameter as a function of nominal P content across all three Si precursors investigated: 100 nm NPs, 500 nm NPs, and 44 μm MPs. The experimental line for crystalline P-doped Si obtained in previous studies[38,39] is shown in black. All materials in panels (a)−(c) were obtained under heating at 5 °C min^{-1}, holding at 1131 °C for 1 h, except open symbols that represent as-received pure Si precursors.

formation of white phosphorus was prevented. The initial dark-brown color of the precursor changed to dark gray as the doping content increased (Figure S1), consistent with previous reports for nanowires.[36,37] The systematic contraction of the Si lattice upon phosphorus substitution was verified by XRD measurements using an internal corundum standard (Figure 1); the change in the lattice parameter closely followed the previously reported trend.[38,39] Together, this is strong evidence of complete or near-complete incorporation of the phosphorus precursor within the silicon phase. Furthermore, the increase in the phosphorus content was further confirmed by measuring the electrical conductivity using a two-probe technique. The properties of SiP_x materials based on 500 nm Si NPs are summarized in Table 1.

Further analysis of the XRD patterns of the homogeneously doped SiP_x materials reveal larger average crystallite size (as calculated by the Scherrer equation) with increasing P content, compared to that of pure 500 nm Si NPs (even when subjected to the same heat treatment at 1131 °C). This effect is corroborated by SEM analysis, showing obvious signs of grain coarsening and faceting of the SiP_x products, especially at high P content (Figure 2).

Raman spectroscopy of the homogeneously doped SiP_x materials reveals a slight decrease in frequency of the Raman-active mode for Si NPs centered at ∼510 cm^{-1} (down to ∼507 cm^{-1}), indicating that the introduction of phosphorus into silicon causes slight amorphization of the crystal structure in the dilute P regime (Figure S2a).[20,40] With increasing P content, however, the peak center shifts back to higher frequency (516 cm^{-1}), indicating higher crystallinity of the resulting materials, as consistent with the XRD analysis. It is important to note that the Raman spectrum varies significantly depending on whether the focus is placed at or below the powder surface; measurements made at the surface (+10 μm from the focus of highest intensity) show a monotonic increase in position from 512 to 516 cm^{-1} with increasing P content, as shown in Figure S2b. This surface/bulk variability decreases significantly in SiP_x samples doped beyond 1.0 at %, indicative of a more homogeneously crystalline structure. Lastly, a significant increase in conductivity was observed in SiP_x NPs as a function of P content (e.g., in the series *xx*P-5R-H-1h, Table 1) as expected for homogeneously P-doped silicon.

https://doi.org/10.1021/acs.chemmater.2c02983
Chem. Mater. 2023, 35, 549−557

Table 1. Materials Properties of SiP_x Derived from 500 nm Si NPs, Grouped by the Synthetic Parameter Varied

synthetic parameter varied	material	Si(111) 2θ (degree)	Si(111) FWHM (degree)	lattice parameter (Å)	crystallite size, L_a (nm)	electrical conductivity (S cm^{-1})
(pristine control)	Si (500 nm)	28.443	0.184	5.4309	8	8.99×10^{-7}
	0.0P-5R-H-1h	28.430	0.112	5.4332	13	4.33×10^{-4}
P content	**0.05P**-5R-H-1h	28.430	0.110	5.4333	14	NM
	0.1P-5R-H-1h	28.440	0.105	5.4313	14	2.06×10^{-2}
	0.2P-5R-H-1h	28.441	0.107	5.4312	14	1.33×10^{-3}
	1.0P-5R-H-1h	28.454	0.064	5.4288	23	1.38×10^{-2}
	3.0P-5R-H-1h	28.481	0.060	5.4237	25	3.85×10^{1}
ramp rate	0.1P-**5R**-H-0h	28.437	0.124	5.4319	12	3.87×10^{-4}
	0.1P-**10R**-H-0h	28.436	0.139	5.4321	11	2.19×10^{-4}
	0.1P-**20R**-H-0h	28.435	0.137	5.4324	11	1.03
	0.1P-**30R**-H-0h	28.435	0.164	5.4323	9	4.99×10^{-2}
	0.1P-**50R**-H-0h	28.440	0.152	5.4314	10	2.21×10^{-1}
temperature	0.1P-5R-**H-0h**	28.437	0.124	5.4319	12	3.87×10^{-4}
	0.1P-5R-**H-1h**	28.440	0.105	5.4313	14	NM
	0.1P-5R-**L-0h**	28.431	0.198	5.4330	8	3.30×10^{-7}
	0.1P-5R-**L-1h**	28.440	0.190	5.4314	8	NM
hold time	0.1P-5R-H-**0h**	28.437	0.120	5.4319	12	3.87×10^{-4}
	0.1P-5R-H-**1h**	28.440	0.105	5.4313	14	3.42
	0.1P-5R-H-**6h**	28.444	0.110	5.4307	14	1.03×10^{1}
	0.1P-5R-H-**12h**	28.434	0.110	5.4326	14	7.51×10^{1}
optimal	0.1P-50R−L-0h	28.436	0.182	5.4319	8	2.80×10^{-7}

While homogeneous solid solutions of SiP_x across the entire solubility range could be achieved by a facile solid-state reaction between Si NPs and red phosphorus, P content and crystallite/particle size were found to be convoluted within this series. To control these effects separately, two additional Si precursors of different nominal particle sizes (100 nm and 44 μm) were also investigated. Similar changes in the lattice parameter, color, and Raman spectral features were observed, as summarized in Table 2 and Figure S3. Hence, these materials were subsequently used to decouple the effects of particle size and P content on the electrochemical behavior of anodes based on silicon NPs and MPs. Additionally, pure 500 nm Si NPs were heat-treated under an inert atmosphere (in identical conditions as for P-doping, except without any phosphorus) to attempt to control for the role of the heat treatment itself on the crystallinity and grain size. Indeed, a slight increase in the crystallite size (from 8 to 13 nm) was observed for heat-treated Si NPs (0.0P-5R-H-1h). However, this effect is much smaller than that observed for heat treatment in the presence of phosphorus (see Figure S3), indicating that the phosphorus precursor itself catalyzed the growth of crystallites and the associated particle size and morphology changes.

3.2. Rapid and Low-Temperature SiP_x Solid Solutions. A second series of experiments were carried out to obtain a wider variety of SiP_x materials for electrochemical analysis. Three strategies were employed to obtain materials with a heterogeneous distribution of the dopant within the silicon lattice: increasing the ramp rate (5−50 °C min^{-1}), decreasing the hold temperature (1131−800 °C), and decreasing the hold time during solid-solution preparation (1−0 h). The properties of the so-obtained materials are summarized in Table 1. This work focuses on dilutely P-doped SiP_x materials (0.1 at %) that are of highest interest to the subsequent electrochemical analyses. Generally, the results reveal that at a fast ramp rate (>30 °C min^{-1}), low temperature (800 °C heat), and short time spent at the highest temperature (0 h hold time), the crystallite size of the resulting material is close to that of pure 500 nm Si NPs.

Raman spectroscopy and SEM analysis further confirm that the silicon morphology and crystallinity are minimally affected under rapid, short hold and low-temperature dissolution conditions. The diffusion of phosphorus within silicon increases from ~2×10^{-18} to 1×10^{-15} m^2 s^{-1} as its concentration increases from 0.1 to 10 at % at 1131 °C.[34,35] An approximate estimate of diffusion depth as a function of time reveals that the homogeneous dissolution of 0.1 at % phosphorus in 500 nm Si NPs requires 5 h to complete. Hence, using ramp rates up to 50 °C min^{-1} and no hold time, a heterogeneously distributed SiP_x solution is expected to result. Importantly, all rapidly doped SiP_x materials exhibit a similar crystal structure to the original Si NPs (Figure S4). There is no enhancement of conductivity when phosphorus is heterogeneously doped at low temperatures (e.g., for 0.1P-50R-L-0h); rather, a significant decrease in conductivity is observed (Table 1). At high temperatures, however, an increase in conductivity can be observed with increasing ramp rate (e.g., for 0.1P-*xx*R-H-0h) and is likely to be attributed to a surface mechanism of these heterogeneous structures. The electrochemical properties of such heterogeneously doped (i.e., surface modified) SiP_x variants are explored and compared to homogeneously doped samples in the following section.

3.3. Electrochemical Studies. Galvanostatic charge−discharge (GCD) cycling was used as the primary means of assessing electrochemical effects related to P-doping (and other concomitant changes to the materials properties such as increased crystallite or particle size) of Si NPs. The samples of highest interest were obtained from 500 nm Si NPs; when not otherwise indicated, all subsequent results relate to SiP_x obtained from this precursor. Electrodes for each sample were prepared using a standard drop-casting method to control for effects such as adhesion and in an effort to make the results widely generalizable to other electrode fabrication techniques (i.e., to ensure as much as possible that the results relate to

https://doi.org/10.1021/acs.chemmater.2c02983
Chem. Mater. 2023, 35, 549−557

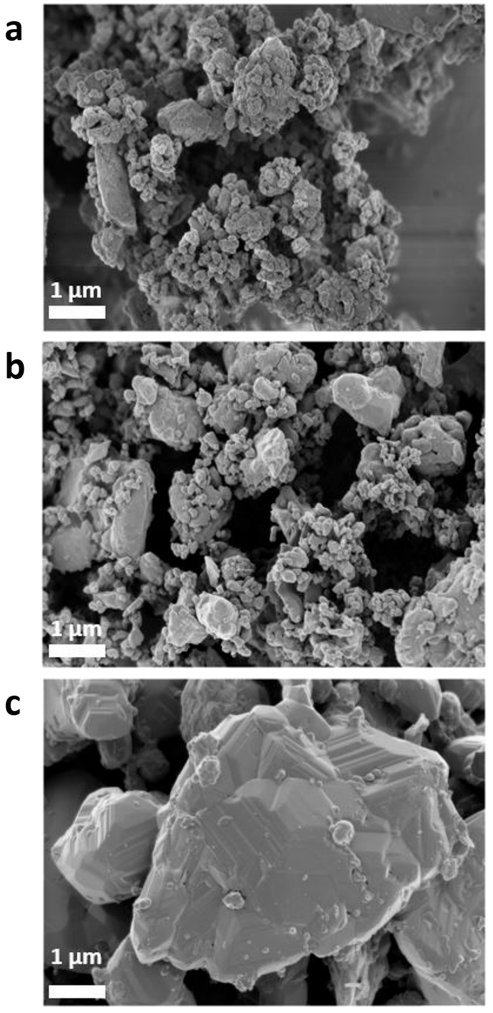

Figure 2. SEM micrographs of (a) as-received pure Si, (b) 0.1 at % SiP_x, and (c) 3.0 at % SiP_x, all obtained from the same precursor: 500 nm Si NPs. The SiP_x materials were obtained under heating at 5 °C min^{-1}, and holding at 1131 °C for 1 h.

materials properties and not to electrode properties). An aqueous binder (CMC) was used and the electrodes were fabricated under air. Half-cells were assembled under inert argon against Li metal as the counter electrode and in flooded electrolyte, in an effort to ensure reproducibility of the results. A standard liquid electrolyte was chosen (1 M $LiPF_6$ in EC/DMC) with a modest amount of FEC (2 wt %) to inhibit excessive SEI (re)formation. Lastly, GCD cycling at a constant current rate of 1 A g^{-1} (~C/3) was employed between 0.05 and 1.5 V vs Li^+/Li to prevent the formation of crystalline $Li_{15}Si_4$.

In all cases, a steep loss of capacity of the SiP_x NPs was observed in the first cycles; this was followed by a less severe decrease in most cases until zero capacity remained (at or before the 200th cycle in all cases herein). In general, cells based on 500 nm NPs were observed to show more significant capacity fading than those based on 100 nm NPs, an expectable effect due to particle size (Figure S5).[3,41] Despite the fact that electrochemical performance was not optimized in this work, this electrode and half-cell formulation allowed for a facile intercomparison between all of the materials investigated and only the relative outcome of each experiment is the focus of discussion herein. The decrease in capacity during initial GCD cycling (1−25 cycles) is attributable to volume expansion and contraction and subsequent loss of electrical contact with a portion of the active SiP_x material. In most cases, this initial capacity loss diminishes for some cycles (showing a seeming approach to a nonzero plateau), and then capacity fade again intensifies until zero capacity is reached. The latter effect is attributable to the formation and nonuniform dissolution of "mossy lithium",[42] which was a well-known failure mechanism in lithium metal batteries.[43] The use of a stable intercalation compound as the counter electrode instead of Li metal (e.g., $LiFePO_4$) would likely resolve the latter issue and will be a focus of future investigations.

3.4. Electrochemical Effects of Homogeneous P-Doping. The GCD voltage profiles of dilutely doped SiP_x materials obtained under conditions that lead to homogeneous doping (i.e., high temperature, long hold time, and slow ramp rate) with P content varying between 0.05 and 0.2 at % are shown in Figures 3a and 4c. The corresponding capacity retention and Coulombic efficiency within the first 200 cycles at up to 1.0 at % is shown in Figure 3d. Higher P content samples (>1.0 at %) did not cycle with any capacity at the benchmark 1 A g^{-1} current employed in this study. All lower concentration SiP_x NPs show comparable second cycle discharge capacities of 2.5−2.9 Ah g^{-1}; materials doped with 1.0 at % P show grievous capacity loss upon cycling, reaching effectively zero capacity within the first 10 cycles. This cycling instability can likely be attributed to a larger crystallite size than the pure Si NPs. This explanation is supported by

Table 2. Materials Properties of SiP_x Derived from 100 nm Si NPs (-n) and 44 μm Si MPs (-μ), Grouped by the Synthetic Parameter Varied

synthetic parameter varied	material	Si(111) 2θ (degree)	Si(111) FWHM (degree)	lattice parameter (Å)	crystallite size, L_a (nm)
P content (100 nm)	Si (100 nm)	28.445	0.290	5.4303	5
	0.0P-5R-H-1h-n	28.450	0.154	5.4294	10
	0.1P-5R-H-1h-n	28.455	0.163	5.4284	9
	2.0P-5R-H-1h-n	28.473	0.060	5.4251	24
	3.0P-5R-H-1h-n	28.484	0.070	5.4230	21
P content (44 μm)	Si (44 μm)	28.425	0.065	5.4343	23
	0.0P-5R-H-1h-μ	28.428	0.062	5.4336	24
	0.05P-5R-H-1h-μ	28.435	0.074	5.4324	20
	0.1P-5R-H-1h-μ	28.435	0.062	5.4323	24
	0.2P-5R-H-1h-μ	28.433	0.081	5.4326	18
	2.0P-5R-H-1h-μ	28.456	0.068	5.4285	22
	3.0P-5R-H-1h-μ	28.468	0.067	5.4262	22

https://doi.org/10.1021/acs.chemmater.2c02983
Chem. Mater. 2023, 35, 549−557

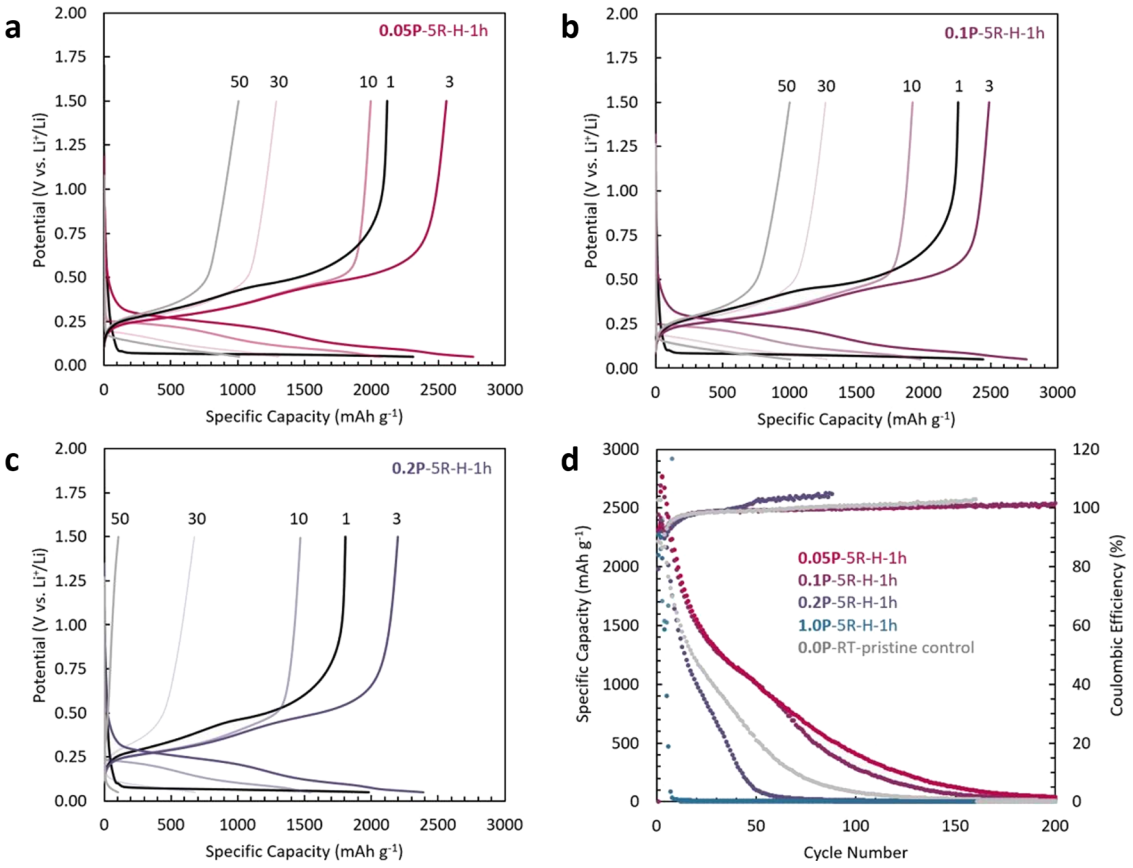

Figure 3. (a–c) GCD lithiation voltage profiles and capacity retention of SiP_x NPs synthesized under homogeneous doping conditions compared to pure Si NPs. Three compositions of highest interest are highlighted: (a) 0.05 at %, (b) 0.1 at %, and (c) 0.2 at % P. The cycle number of each profile is indicated. (d) GCD lithiation capacity retention and Coulombic efficiency of homogeneously doped SiP_x NPs.

comparison to the cycling instability of pure Si MPs (Figure S5). On the other hand, SiP_x NPs in the most dilute doping regime (≤0.1 at % P) exhibited higher cycling stability than the pure Si NPs. It is important to note that this difference in stability cannot be attributed to significant lattice contraction or to smaller crystallite size (see Table 1) and therefore must be owed to the presence of P in the lattice. Slower ramp rates and longer hold times during phosphorus dissolution in general give rise to larger crystallites and grain coarsening, and therefore to poorer cycling stability. It remains unknown whether, if higher concentration SiP_x NPs could be prepared at the same particle size as the native Si NPs, they would show longer cycling stability yet than the low P content SiP_x NPs that exhibit the longest cycling stability in this study.

3.5. Electrochemical Effects of Heterogeneous P-Doping. SiP_x NPs prepared using fast ramp rates, short hold times, and low dissolution temperatures generally exhibit improved capacity compared to pristine 500 nm Si NPs. The effect of ramp rate (at 5, 10, 20, and 50 °C min^{-1}) on cycling retention is shown in Figure 4a. SiP_x NPs obtained at fast ramp rates (≥20 °C min^{-1}) maintain crystallite sizes (L_a = 9–11 nm) comparable to pure Si NPs (L_a = 8 nm) (see Table 1) and also exhibit the highest capacity retention. The effect of hold time (for 0, 1, 6, and 12 h) on capacity retention is shown in Figure 4b. SiP_x NPs with the least amount of hold time (0 and 1 h) exhibit high capacity and stability compared to pure Si NPs, whereas longer hold times (6 and 12 h) result in earlier capacity fading, worse than that exhibited by pure Si NPs. Interestingly, pure Si NPs held at 0, 1, 6, or 12 h hold times (i.e., annealed at 1131 °C) exhibit no difference in the electrochemical behavior (Figure S6) or in the crystallite size (Figure S7) than pristine Si NPs. This is strong evidence that the addition of phosphorus to the Si NPs is the primary cause for grain coarsening via a catalytic (crystallization) effect, leading to poor capacity retention when present at high concentrations. Lastly, the effect of dissolution temperature (at 800 or 1000 °C) on capacity retention is shown in Figure 4c. Based on the equilibrium binary Si–P phase diagram, a temperature of 800 °C is, in principle, sufficient to achieve a doping of 0.3 at % P.[33] Based on GCD cycling analysis, SiP_x NPs synthesized at a lower temperature (800 °C) with no hold time (0 h) exhibit the highest capacity and cycling stability compared to SiP_x materials synthesized at higher temperatures and also retain an extremely small crystallite size (L_a = 8 nm) equivalent to pure Si NPs. Interestingly, such heterogeneously doped SiP_x materials in general do not exhibit improved electrical conductivity compared to pure Si (Table 1). Hence, the role of improved electrical conductivity as the sole reason for improved capacity retention can be ruled out by these results.

The consequences of P-doping toward thermal stability were preliminarily explored by TGA experiments of the bare SiP_x material under flowing air up to 1100 °C. In general, P-doping was observed to increase the thermal decomposition temperature, though the effects were difficult to decouple from grain coarsening (i.e., reduction in the surface area) effects. The results are shown in Figure S8. Further analysis of the thermal stabilizing effects of P-doping on SiP_x anodes will be carried

https://doi.org/10.1021/acs.chemmater.2c02983
Chem. Mater. 2023, 35, 549–557

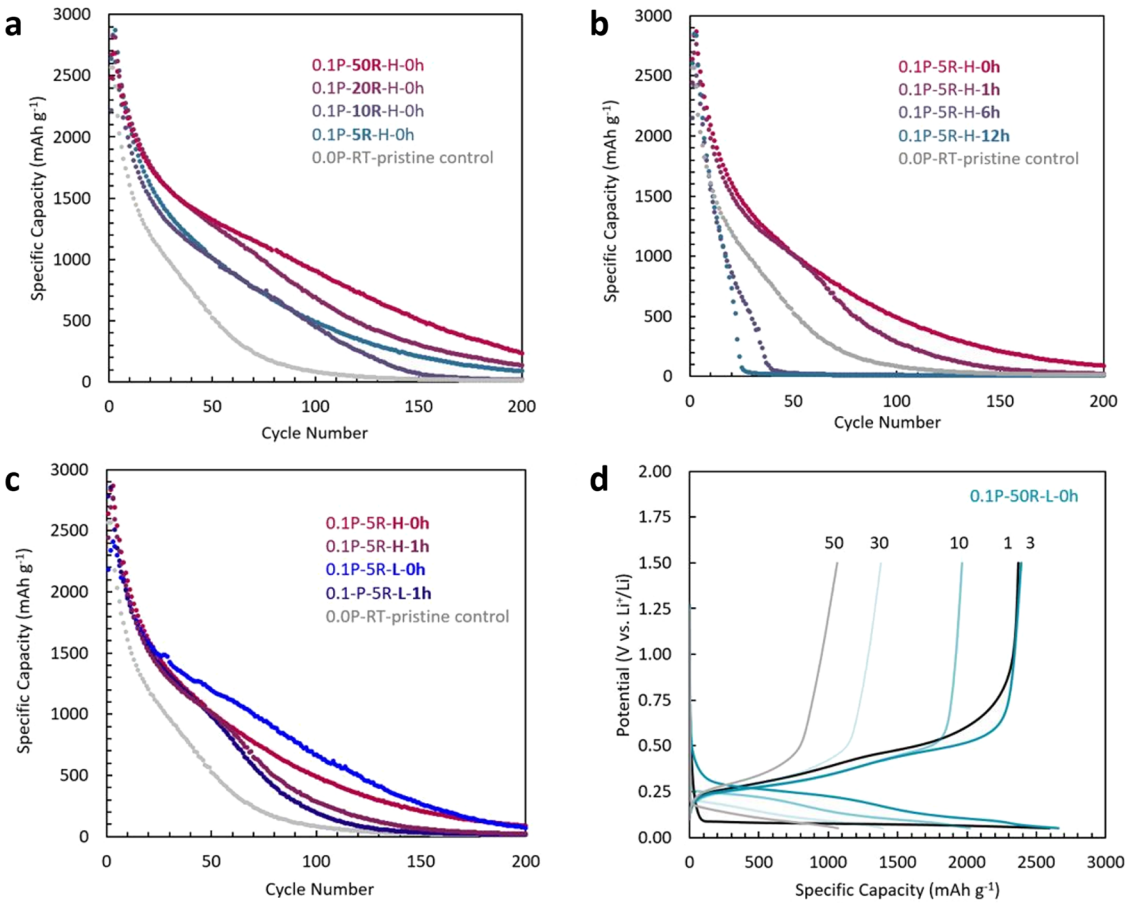

Figure 4. (a–c) GCD lithiation capacity retention of SiP_x NPs synthesized under heterogeneous doping conditions. The effects of (a) ramp rate, (b) hold time, and (c) high temperature are shown for comparison to pure Si NPs. (d) GCD lithiation voltage profiles of SiP_x NPs synthesized under optimal heterogeneous conditions. The cycle number of each profile is indicated.

out in future work in the presence of carbonate electrolytes of highest interest to technological applications.

4. DISCUSSION

This work focuses on determining the sole effects of P-doping on the electrochemical (and thermal) stability of Si, independent of the effects due to altering particle morphology/size, in a standard liquid-electrolyte cell configuration (i.e., neglecting to optimize for the electrolyte, binder, and other additives). Standard electrode fabrication methods (powder active material, liquid slurry casting, and vacuum drying in air) were favored, requiring P-doping of existing Si nano- and micropowders. This is distinct from previous investigations of P-doped silicon electrodes prepared by a gas deposition (GD) method.[20] Correspondingly, there is a significant difference in the results. While Domi and co-workers reported monotonically increasing electrochemical stability (cycling retention) as a function of P content, this work reveals a trade-off between P content and particle size/crystallinity that results in a maximum electrochemical stability at an intermediate P content. Remarkably, both studies favor an optimal P content around 0.1 at % (though in the GD-prepared electrodes, this was the highest P content investigated). Further differences are revealed in the effects of P-doping on lithiation capacity. In this work, initial capacities within the first several cycles did not vary significantly as a function of P-doping; the effects of P-doping (and likewise of crystallite and particle size) were only revealed in terms of capacity retention. In other words, P-doping did not restrict the ultimate lithiation capacity of silicon. In the results reported by Domi and co-workers, P-doping seemed to decrease the ultimate lithiation capacity of GD-prepared electrodes, though cycling retention was improved. These differences persist despite both studies using the same current rate of 1 A g^{-1}. Other past studies (theoretical and experimental) of P-doping silicon anodes for LIBs place a high emphasis on the effects due to enhanced electrical conductivity over that of pure silicon.[44,45] Interestingly, while an increase in conductivity as a function of P-doping was measured and might help explain electrochemical differences within the homogeneously doped (e.g., *xx*P-5R-H-1h) series in this work, only very low conductivities were measured in the heterogeneously doped samples that had the highest overall electrochemical stability (e.g., 0.1P-50R-L-0h). Hence, we cannot attribute improved electrochemical stability to increased conductivity within the range of conditions explored herein, and future work is needed to decouple these properties.

Within the synthetic conditions explored in this study, low P content (≤0.1 at % P), fast ramp rate (e.g., 50 °C min^{-1}), short hold time (0 h), and low dissolution temperature (800 °C) together give rise to the highest capacity retention of SiP_x NPs within the electrochemical conditions of interest in this study: ~C/3 cycling between 0.05 and 1.5 V vs Li^+/Li in a standard carbonate electrolyte. The low phosphorus concentrations inherent to the top-performing materials within each para-

https://doi.org/10.1021/acs.chemmater.2c02983
Chem. Mater. 2023, 35, 549–557

metric study (typically 0.1 at % P) make direct confirmation of the homogeneity of doping a significant challenge. Two methods were attempted to be used herein: X-ray photoelectron spectroscopy (XPS) and time-of-flight secondary ion mass spectrometry (TOF-SIMS). Unfortunately, neither method was reliably successful at determining the P content homogeneity as a function of depth below the NP surface. Nevertheless, there is strong evidence in the overall body of work reported herein that a heterogeneous distribution of dilute phosphorus within SiP_x NPs (possibly a core−shell structure) is favorable for capacity retention in LIB anode applications. Future work should be performed to explore the origin of these effects.

5. CONCLUSIONS

Homogeneous and heterogeneous doping of phosphorus within silicon NPs was achieved by varying a wide range of synthetic parameters. A standard top-down solid-state dissolution route was employed allowing for facile fine tuning of the final SiP_x product; the most important goal of this work was to determine the role of phosphorus substitution within the silicon lattice on electrochemical charge/discharge stability, as decoupled from other properties such as particle size and distribution of the dopant. To this end, it has been shown that phosphorus substitution does in fact significantly improve the electrochemical stability of Si NPs in a standard LIB liquid electrolyte. A primary result of this study is that doping at 0.05−0.1 at % P gives rise to optimal charge storage capacity and cycling stability. Further improvement can be gained by enforcing a heterogeneous distribution of the dopant; dilute doping in the NP shell/surface region via low-temperature set point (800 °C), no hold time (0 h), and fast ramp rate (50 °C min^{-1}) give rise to optimal electrochemical cycling stability overall. Elucidation of the precise distribution of phosphorus within the SiP_x NPs remains an important aspect of future work.

■ ASSOCIATED CONTENT

Supporting Information

The Supporting Information is available free of charge at https://pubs.acs.org/doi/10.1021/acs.chemmater.2c02983.

Further XRD and Raman characterization, electrochemical characterization, thermal analysis, and photographs of SiP_x powders (PDF)

■ AUTHOR INFORMATION

Corresponding Author

Nicholas P. Stadie − *Materials Science Program, Montana State University, Bozeman, Montana 59717, United States; Department of Chemistry & Biochemistry, Montana State University, Bozeman, Montana 59717, United States;* orcid.org/0000-0002-1139-7846; Email: nstadie@montana.edu

Authors

Isabelle P. Gordon − *Materials Science Program, Montana State University, Bozeman, Montana 59717, United States*

Wei Xu − *Department of Chemistry & Biochemistry, Montana State University, Bozeman, Montana 59717, United States*

Sophia Randak − *Department of Chemistry & Biochemistry, Montana State University, Bozeman, Montana 59717, United States*

T. Richard Jow − *Battery Science Branch, Energy Sciences Division, Army Research Directorate, DEVCOM Army Research Laboratory, Adelphi, Maryland 20783, United States;* orcid.org/0000-0003-1615-8593

Complete contact information is available at: https://pubs.acs.org/10.1021/acs.chemmater.2c02983

Notes

The authors declare no competing financial interest.

■ ACKNOWLEDGMENTS

The authors thank Seth Kane for assistance in performing the electrical conductivity measurements (and access to the instrumentation), Emanuel Billeter for performing the ill-fated XPS experiments, and Alex Naglich for performing the ill-fated TOF-SIMS experiments. The authors also thank the Montana Nanotechnology Facility (MONT, an NNCI facility supported by the National Science Foundation Grant ECCS-1542210) and the Center for Biofilm Engineering Imaging Facility (RaSCAL, a user facility supported by the National Science Foundation Grant DBI-1726561 and the M.J. Murdock Charitable Trust Grant SR-2017331) for use of their instrumentation. Funding for this work was provided by the DEVCOM Army Research Laboratory (ARL) under cooperative agreement (W911NF-20-2-0284).

■ REFERENCES

(1) Franco Gonzalez, A.; Yang, N.-H.; Liu, R.-S. Silicon Anode Design for Lithium-Ion Batteries: Progress and Perspectives. *J. Phys. Chem. C* **2017**, *121*, 27775−27787.

(2) Liu, N.; Huo, K.; McDowell, M. T.; Zhao, J.; Cui, Y. Rice Husks as a Sustainable Source of Nanostructured Silicon for High Performance Li-Ion Battery Anodes. *Sci. Rep.* **2013**, *3*, No. 1919.

(3) Domi, Y.; Usui, H.; Sugimoto, K.; Sakaguchi, H. Effect of Silicon Crystallite Size on its Electrochemical Performance for Lithium-Ion Batteries. *Energy Technol.* **2019**, *7*, No. 1800946.

(4) Liu, X. H.; Zhong, L.; Huang, S.; Mao, S. X.; Zhu, T.; Huang, J. Y. Size-Dependent Fracture of Silicon Nanoparticles During Lithiation. *ACS Nano* **2012**, *6*, 1522−1531.

(5) Peng, K.; Jie, J.; Zhang, W.; Lee, S.-T. Silicon Nanowires for Rechargeable Lithium-Ion Battery Anodes. *Appl. Phys. Lett.* **2008**, *93*, No. 033105.

(6) Chan, C. K.; Peng, H.; Liu, G.; McIlwrath, K.; Zhang, X. F.; Huggins, R. A.; Cui, Y. High-Performance Lithium Battery Anodes Using Silicon Nanowires. *Nat. Nanotechnol.* **2008**, *3*, 31−35.

(7) Xu, Y.; Yin, G.; Ma, Y.; Zuo, P.; Cheng, X. Nanosized Core/Shell Silicon@Carbon Anode Material for Lithium Ion Batteries with Polyvinylidene Fluoride as Carbon Source. *J. Mater. Chem.* **2010**, *20*, 3216−3220.

(8) Huang, S.; Cheong, L. Z.; Wang, D.; Shen, C. Nanostructured Phosphorus Doped Silicon/Graphite Composite as Anode for High-Performance Lithium-Ion Batteries. *ACS Appl. Mater. Interfaces* **2017**, *9*, 23672−23678.

(9) Profatilova, I. A.; Langer, T.; Badillo, J. P.; Schmitz, A.; Orthner, H.; Wiggers, H.; Passerini, S.; Winter, M. Thermally Induced Reactions between Lithiated Nano-Silicon Electrode and Electrolyte for Lithium-Ion Batteries. *J. Electrochem. Soc.* **2012**, *159*, A657−A663.

(10) Wang, Y.; Dahn, J. R. Comparison of the Reactions Between Li_xSi or $Li_{0.81}C_6$ and Nonaqueous Solvent or Electrolytes at Elevated Temperature. *J. Electrochem. Soc.* **2006**, *153*, No. A2188.

(11) Yoon, T.; Milien, M. S.; Parimalam, B. S.; Lucht, B. L. Thermal Decomposition of the Solid Electrolyte Interphase (SEI) on Silicon Electrodes for Lithium Ion Batteries. *Chem. Mater.* **2017**, *29*, 3237−3245.

(12) Yang, G.; Frisco, S.; Tao, R.; Philip, N.; Bennett, T. H.; Stetson, C.; Zhang, J.-G.; Han, S.-D.; Teeter, G.; Harvey, S. P.; Zhang, Y.;

Veith, G. M.; Nanda, J. Robust Solid/Electrolyte Interphase (SEI) Formation on Si Anodes Using Glyme-Based Electrolytes. *ACS Energy Lett.* **2021**, *6*, 1684−1693.
(13) Ababtain, K.; Babu, G.; Lin, X.; Rodrigues, M. T.; Gullapalli, H.; Ajayan, P. M.; Grinstaff, M. W.; Arava, L. M. Ionic Liquid-Organic Carbonate Electrolyte Blends To Stabilize Silicon Electrodes for Extending Lithium Ion Battery Operability to 100 Degrees C. *ACS Appl. Mater. Interfaces* **2016**, *8*, 15242−15249.
(14) Xu, K.; Wang, C. Batteries: Widening Voltage Windows. *Nat. Energy* **2016**, *1*, No. 16161.
(15) Tan, D. H. S.; Chen, Y.; Yang, H.; Bao, W.; Sreenarayanan, B.; Doux, J.; Li, W.; Lu, B.; Ham, S.; Sayahpour, B.; Scharf, J.; Wu, E.; Deysher, G.; Han, H.; Hah, H.; Jeong, H.; Lee, J.; Chen, Z.; Meng, Y. Carbon-Free High-Loading Silicon Anodes Enabled by Sulfide Solid Electrolytes. *Science* **2021**, *373*, 1494−1499.
(16) Chen, M.; Li, B.; Liu, X.; Zhou, L.; Yao, L.; Zai, J.; Qian, X.; Yu, X. Boron-Doped Porous Si Anode Materials with High Initial Coulombic Efficiency and Long Cycling Stability. *J. Mater. Chem. A* **2018**, *6*, 3022−3027.
(17) Li, P.; Hwang, J. Y.; Sun, Y. K. Nano/Microstructured Silicon-Graphite Composite Anode for High-Energy-Density Li-Ion Battery. *ACS Nano* **2019**, *13*, 2624−2633.
(18) Ren, Y.; Zhou, X.; Tang, J.; Ding, J.; Chen, S.; Zhang, J.; Hu, T.; Yang, X. S.; Wang, X.; Yang, J. Boron-Doped Spherical Hollow-Porous Silicon Local Lattice Expansion toward a High-Performance Lithium-Ion-Battery Anode. *Inorg. Chem.* **2019**, *58*, 4592−4599.
(19) Qu, X.; Zhang, X.; Wu, Y.; Hu, J.; Gao, M.; Pan, H.; Liu, Y. An Eggshell-Structured N-Doped Silicon Composite Anode with High Anti-Pulverization and Favorable Electronic Conductivity. *J. Power Sources* **2019**, *443*, No. 227265.
(20) Domi, Y.; Usui, H.; Shimizu, M.; Kakimoto, Y.; Sakaguchi, H. Effect of Phosphorus-Doping on Electrochemical Performance of Silicon Negative Electrodes in Lithium-Ion Batteries. *ACS Appl. Mater. Interfaces* **2016**, *8*, 7125−7132.
(21) Long, B.; Zou, Y.; Li, Z.; Ma, Z.; Jiang, W.; Zou, H.; Chen, H. Effect of Phosphorus Doping on Conductivity, Diffusion, and High Rate Capability in Silicon Anode for Lithium-Ion Batteries. *ACS Appl. Energy Mater.* **2020**, *3*, 5572−5580.
(22) Ette, P. M.; Bhargav, P. B.; Ahmed, N.; Chandra, B.; Rayarfrancis, A.; Ramesha, K. Nanocrystalline Silicon Embedded Highly Conducting Phosphorus Doped Silicon Thin Film as High Power Lithium Ion Battery Anode. *Electrochim. Acta* **2020**, *330*, No. 135318.
(23) Chen, M.; Zhou, Q.; Zai, J.; Iqbal, A.; Tsega, T.; Dong, B.; Liu, X.; Zhang, Y.; Yan, C.; Zhao, L.; Nazakat, A.; E, S.; Low, C.; Qian, X. High Power and Stable P-Doped Yolk-Shell Structured Si@C Anode Simultaneously Enhancing Conductivity and Li+ Diffusion Kinetics. *Nano Res.* **2021**, *14*, 1004−1011.
(24) Tang, F.; Tan, Y.; Jiang, T.; Zhou, Y. Phosphorus-Doped Silicon Nanoparticles as High Performance LIB Negative Electrode. *J. Mater. Sci.* **2022**, *57*, 2803−2812.
(25) Ryu, J.; Seo, J. H.; Song, G.; Choi, K.; Hong, D.; Wang, C.; Lee, H.; Lee, J. H.; Park, S. Infinitesimal Sulfur Fusion Yields Quasi-Metallic Bulk Silicon For Stable and Fast Energy Storage. *Nat. Commun.* **2019**, *10*, No. 2351.
(26) Han, B.; Liao, C.; Dogan, F.; Trask, S. E.; Lapidus, S. H.; Vaughey, J. T.; Key, B. Using Mixed Salt Electrolytes to Stabilize Silicon Anodes for Lithium-Ion Batteries via in Situ Formation of Li-M-Si Ternaries (M = Mg, Zn, Al, Ca). *ACS Appl. Mater. Interfaces* **2019**, *11*, 29780−29790.
(27) Baran, V.; van Wullen, L.; Fassler, T. F. Substitution of Lithium for Magnesium, Zinc, and Aluminum in $Li_{15}Si_4$: Crystal Structures, Thermodynamic Properties, as well as ^{6}Li and ^{7}Li NMR Spectroscopy of $Li_{15}Si_4$ and $Li_{15-x}M_xSi_4$ (M = Mg, Zn, and Al). *Chem. - Eur. J.* **2016**, *22*, 6598−6609.
(28) Trumbore, F. A. Solid Solubilities of Impurity Elements in Germanium and Silicon. *Bell Syst. Tech. J.* **1960**, *39*, 205−233.
(29) Thurber, W. R.; Mattis, R. L.; Liu, Y. M.; Filliben, J. J. Resistivity-Dopant Density Relationship for Boron-Doped Silicon. *J. Electrochem. Soc.* **1980**, *127*, 2291−2294.
(30) Spear, W. E.; Le Comber, P. G. Substitutional Doping of Amorphous Silicon. *Solid State Commun.* **1975**, *17*, 1193−1196.
(31) Daali, A.; Zhao, C.; Zhou, X.; Yang, Z.; Amine, R.; Liu, Y.; Wilkistar, O.; Xu, G.-L.; Amine, K. Tuning Working Potential of Silicon-Phosphorus Anode via Microstructure Control for High-Energy Lithium-Ion Batteries. *J. Solid State Electrochem.* **2022**, *26*, 1919−1927.
(32) Kane, S.; Warnat, S.; Ryan, C. Improvements in Methods for Measuring the Volume Conductivity of Electrically Conductive Carbon Powders. *Adv. Powder Technol.* **2021**, *32*, 702−709.
(33) Olesinski, R. W.; Kanani, N.; Abbascian, G. J. The P-Si (Phosphorus-Silicon) System. *Bull. Alloy Phase Diagrams* **1985**, *6*, 130−133.
(34) Jones, S. W. Diffusion in Silicon, 2008. www.icknowledge.com (accessed Dec 18, 2022).
(35) Fuller, C. S.; Ditzenberger, J. A. Diffusion of Boron and Phosphorus into Silicon. *J. Appl. Phys.* **1954**, *25*, 1439−1440.
(36) Canham, L. T. *Handbook of Porous Silicon*; Springer: Switzerland, 2014.
(37) Cao, L.; Fan, P.; Barnard, E. S.; Brown, A. M.; Brongersma, M. L. Tuning the Color of Silicon Nanostructures. *Nano Lett.* **2010**, *10*, 2649−2654.
(38) Pearson, G. L.; Bardeen, J. Electrical Properties of Pure Silicon and Silicon Alloys Containing Boron and Phosphorus. *Phys. Rev.* **1949**, *75*, 865−883.
(39) McQuhae, K. G.; Brown, A. S. The Lattice Contraction Coeffecient of Boron and Phosphorus in Silicon. *Solid-State Electron.* **1972**, *15*, 259−264.
(40) Meng, C.-Y.; Chen, J.-L.; Lee, S.-C.; Chia, C.-T. Doping Effects on the Raman Spectra of Silicon Nanowires. *Phys. Rev. B* **2006**, *73*, No. 245309.
(41) Li, H.; Huang, X.; Chen, L.; Wu, Z.; Liang, Y. A High Capacity Nano-Si Composite Anode Material for Lithium Rechargable Batteries. *Electrochem. Solid-State Lett.* **1999**, *2*, No. 547.
(42) Orsini, F.; Du Pasquier, A.; Beaudoin, B.; Tarascon, J. M.; Trentin, M.; Langenhuizen, N.; De Beer, E.; Notten, P. In Situ Scanning Electron Microscopy (SEM) Observations of Interfaces within Plastic Lithium Batteries. *J. Power Sources* **1998**, *76*, 19−29.
(43) Cohen, Y. S.; Cohen, Y.; Aurbach, D. Micromorphological Studies of Lithium Electrodes in Alkyl Carbonate Solutions Using In Situ Atomic Force Microscopy. *J. Phys. Chem. B* **2000**, *104*, 12282−12291.
(44) Long, B. R.; Chan, M. K. Y.; Greeley, J. P.; Gewirth, A. A. Dopant Modulated Li Insertion in Si for Battery Anodes: Theory and Experiment. *J. Phys. Chem. C* **2011**, *115*, 18916−18921.
(45) Arie, A. A.; Lee, J. K.Electrochemical Properties of P-Doped Silicon Thin Film Anodes of Lithium Ion Batteries. In *Materials Science Forum*; Trans Tech Publications Ltd., 2013; Vol. *737*, pp 80−84.